Geomechanics and Engineering, *Vol. 11*, *No. 3* (*2016*) *325-343*
DOI: http://dx.doi.org/10.12989/gae.2016.11.3.325

An elastoplastic bounding surface model for the cyclic undrained behaviour of saturated soft clays

Xinglei Cheng and Jianhua Wang*

State Key Laboratory of Hydraulic Engineering Simulation and Safety of Tianjin University, *Tianjin University*, *Tianjin 300072*, *P.R. China*

(*Received May 29*, *2015*, *Revised January 13*, *2016*, *Accepte May 01*, *2016*)

Abstract. A total stress-based bounding surface model is developed to predict the undrained behaviour of saturated soft clays under cyclic loads based on the anisotropic hardening modulus field and bounding-surface theories. A new hardening rule is developed based on a new interpolation function of the hardening modulus that has simple mathematic expression and fewer model parameters. The evolution of hardening modulus field is described in the deviatoric stress space. It is assumed that the stress reverse points are the mapping centre points and the mapping centre moves with the variation of loading and unloading paths to describe the cyclic stress-strain hysteresis curve. In addition, by introducing a model parameter that reflects the accumulation rate and level of shear strain to the interpolation function, the cyclic shakedown and failure behaviour of soil elements with different combinations of initial and cyclic stresses can be captured. The methods to determine the model parameters using cyclic triaxial compression tests are also studied. Finally, the cyclic triaxial extension and torsional shear tests are performed. By comparing the predictions with the test results, the model can be used to describe undrained cyclic stress-strain responses of elements with different stress states for the tested clays.

Keywords: soft clay; constitutive model; cyclic loading; hardening modulus field; bounding surface

1. Introduction

Many marine engineering structures such as deep-water suction anchors and large- diameter bucket foundations must be built on the seabed soft-clay foundation (Chen and Randolph 2007, Andersen 2009). They are put into operation immediately after a short-time on-site installation (API RP2A-WSD 2002). Because of low permeability, the soft clays around foundation are basically in undrained states when they are subjected to the working loads and cyclic loads from wind and waves. For this case, the yielding of soft clays is independent of normal total stress and only depends on deviatoric stress (Prevost 1977, Borja and Amies 1994, Anastasopoulos *et al*. 2011, Huang and Liu 2014). During the soil-structural interaction analysis, the undrained soft-clay can be regarded as single-phase medium materials, and then the deviatoric deformation under cyclic loading can be calculated by using a total stress-based model to simplify the calculation process.

The constitutive models describing stress-strain behaviour of soft clays under cyclic loads have

*Corresponding author, Professor, E-mail: tdwjh@tju.edu.cn

http://www.techno-press.org/?journal=gae&subpage=7 ISSN: 2005-307X (Print), 2092-6219 (Online)

been broadly divided into two categories, ones are effective stress-based constitutive models, the others are total stress-based constitutive models. For the former, more researches have been carried out (Mroz *et al*. 1981, Dafalias and Herrmann 1982, 1986, Pande and Pietruszczak 1982, Tabbaa and Wood 1989, Liang and Ma 1992, Crouch and Wolf 1994, Li and Meissne 2002, Yu *et al*. 2007, Huang *et al*. 2009, 2011, Hu *et al*. 2012, Kimoto *et al*. 2013, Yin *et al*. 2013, Seidalinov and Taiebat 2014, Hong *et al*. 2014, Ni *et al*. 2015). Such models describe the deformation and failure of soft clays from the perspective of effective stress based on the critical state theory. The models often involve complex interpolation functions of plastic modulus and hardening rules. Too many model parameters are required and the volume change constraints or the consolidation equation need to be introduced to carry out the finite element analysis in undrained condition, which make the models difficult for numerical implementation. Comparing to the former, researches about the latter are relatively less (Prevost 1977, Borja and Amies 1994, Wang and Yao 1996, Xiong and Chen 2008, Anastasopoulos *et al*. 2011, Huang and Liu 2014). For total stress-based models for saturated soft clays, hardening modulus field is generally constructed in the deviatoric stress space, and then the relationship between the deviatoric stress increment and the deviatoric strain increment is built. Since the total stress-based models involve only the hardening mechanism of plastic deviatoric strain, the expression of hardening modulus is relatively simple and model parameters are relatively less, which make them easier to be implemented into 3D finite-element codes. However, phenomena such as pore-pressure buildup and dissipation cannot possibly be captured.

Although the models proposed in the form of effective stress or total stress can describe the basic mechanical properties of soil subjected to cyclic loading such as non-linear, hysteresis and strain accumulation to some extent, there are some inadequateness, that is the models are validated only in a particular stress state, such as the models proposed by Dafalias (Dafalias and Herrmann) 1982, Li and Meissne 2002, Yu *et al*. 2007, Huang *et al*. 2009, 2011, Hu *et al*. 2012, Ni *et al*. 2015 have only been verified under triaxial stress states, the applicability of other stress states is unknown. Besides, model parameters match with only a particular stress conditions, and then can only predict the stress-strain response of the soil element in a particular stress condition, once the stress conditions of soil element change, the model parameters must be redetermined. Such as the two-surface model proposed by Li and Meissne need two different sets of model parameters to predict test results of one-way and two-way cyclic triaxial loading. For Yu's model, during determining hardening modulus for reloading stress path, the parameter controlling the shakedown behaviour of the soil is not constant, and it is dependent upon many factors including the cyclic stress history and the current stress level of the soil, which leads to the value of parameter must be redetermined to predict the test results in different stress conditions; Another example is Huang's model, the model parameters in the interpolation function of plastic modulus are determined using trial-and-error simulations of the stress-strain curve test results, thus whether the model parameters determined in this way can be suitable for other stress condition remains to be further studied. Obviously, the model parameters determined by a particular stress condition tend to have certain limitations. They can't comprehensively reflect the effect of the initial stress levels, cyclic stress levels and number of stress cycles on the stress-strain responses of the soil, so they can't describe the stress-strain responses of soil elements in general stress states. However, only the model parameters have universal applicability for soil elements in general stress states, can the model be applied to solve the boundary value problem, which is the purpose of this study.

Based on the above analysis, the main objective of this paper is to develop a total stress-based constitutive model that is suitable for analysing the deformation of soft clays subjected to cyclic

loads. A new hardening rule is developed based on the anisotropic hardening modulus field and bounding-surface theories, the evolutions of hardening modulus is described in the deviatoric stress space by the movement of mapping centre to describe the cyclic hysteretic stress-strain responses. The variation of hysteresis curves is controlled by introducing a model parameter reflecting the accumulation rate and level of shear strain to the interpolation function of elastoplastic modulus. The methods to determine the model parameters using cyclic triaxial compression tests are discussed in details in the present work. Furthermore, the stress-strain responses of the tested clays under cyclic triaxial tensile and torsional shear stress states are predicted to verify the applicability of the model for soil elements with different stress states.

2. Elastoplastic bounding surface model

The development of incremental elastoplastic models based on the anisotropic hardening modulus field and bounding surface theories mainly include three aspects: the bounding surface equation, which describes the failure of the soil element; the evolution rules of the hardening modulus; and the incremental elastoplastic stress-strain relationship.

2.1 Bounding surface equation

The ultimate strength of the soil element is characterised by the bounding surface, and failure occurs when the stress point reaches the bounding surface. Since during unconsolidated undrained loading, the yielding and failure of soft clay is independent of the imposed normal total stress component, only depends on the deviatoric stress (Prevost 1977, Li 2004, Wang and Qu 2011). thus, the bounding surface equation is represented by simple Von Mises yield criterion

$$F = \frac{3}{2}\bar{s}_{ij}\bar{s}_{ij} - A_0^2 = 0 \tag{1}$$

where $\bar{s}_{ij}$ denotes the deviatoric stress tensor, and A_0 denotes the radius of the bounding surface.

When cylindrical coordinate is used to represents the bounding surface equation, if the stress state of soil element satisfies $\bar{\sigma}_z \neq \bar{\sigma}_r = \bar{\sigma}_\theta$, $\bar{\tau}_{rz} \neq \bar{\tau}_{r\theta} = 0$, Eq. (1) can be simplified to

$$F = (\bar{\sigma}_z - \bar{\sigma}_\theta)^2 + 3\bar{\tau}_{z\theta}{}^2 - A_0{}^2 = 0 \tag{2}$$

In Eq. (2), $\bar{\sigma}_z$, $\bar{\sigma}_\theta$, and $\bar{\tau}_{z\theta}$ denote the axial normal stress, circumferential normal stress and circumferential shear stress, respectively.

If the stress state of the soil element satisfies $\bar{\sigma}_z = \bar{\sigma}_r = \bar{\sigma}_\theta$, $\bar{\tau}_{rz} \neq \bar{\tau}_{r\theta} = 0$, Eq. (1) can be simplified to

$$F = 3\bar{\tau}_{z\theta}{}^2 - A_0{}^2 = 0 \tag{3}$$

If the soil element is in the triaxial stress state, $\bar{\sigma}_\theta = \bar{\sigma}_r$, and $\bar{\tau}_{z\theta} = \bar{\tau}_{\theta r} = \bar{\tau}_{rz} = 0$, the bounding surface Eq. (1) can be further simplified to

$$F = \left(\bar{\sigma}_z - \bar{\sigma}_\theta\right)^2 - A_0^2 = 0 \tag{4}$$

If we assume $\bar{\sigma}_R = \bar{\sigma}_z - \bar{\sigma}_\theta$, Eq. (4) is simplified to

$$F = \left(\bar{\sigma}_R\right)^2 - A_0^2 = 0 \tag{5}$$

2.2 Evolution rule of the hardening modulus field

Here, the evolution rules of the hardening modulus field are elaborated using bounding surface Eq. (2). In this case, the bounding surface is a circle of radius A_0 in a $\sigma_z - \sigma_\theta$ versus $\sqrt{3}\tau_{z\theta}$ stress plane as shown in Figs. 1(a) and (b). During the triaxial tests, the shear stress components is $\tau_{z\theta} = 0$, and the stress point continues moving consistently along the σ_R-axis. A typical stress-strain curve obtained in the triaxial compression tests is shown in Fig. 1(c). The maximum modulus of the stress-strain curve is obtained at the initial loading and can be represented as the maximum elastoplastic modulus $H_{\max}$. Failure occurs for the soil element when the stress point reaches the bounding surface. At this exact moment, the modulus should approach zero, which is denoted as $H = 0$.

The mapping rule for initial loading is schematically shown in Fig. 1(a), where s_R^0, s_R' and s_R denote the initial loading point, stress reversal point, and current stress point, respectively; $\bar{s}_R$ denotes the image stress point, which is the intersection point of the bounding surface and a line passing through the initial loading stress and current stress point. The position of each point in the

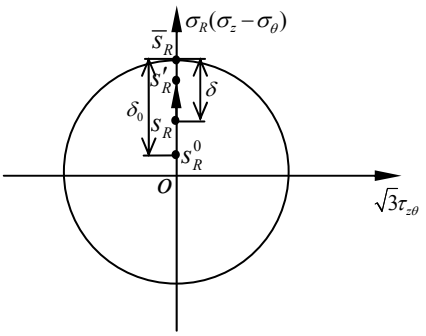

(a) Mapping rule for initial loading

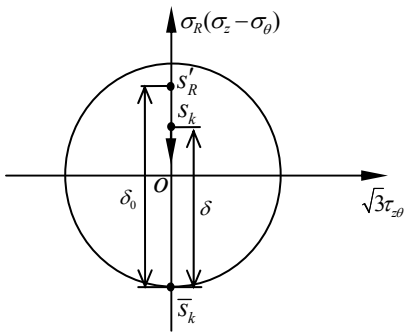

(b) Mapping rule for unloading

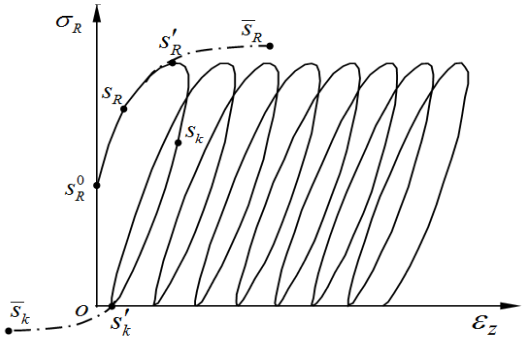

(c) Typical stress strain curve for cyclic triaxial tests

Fig. 1 Illustration of the mapping rule for loading and unloading

stress-strain curve is shown in Fig. 1(c). Here, the loading path abruptly changes direction at the stress reversal point. For the general three-dimensional stress states, it is assumed that the stress path reverses when the dot product between the deviatoric stress increment vector of the current stress point and the exterior normal vector of the bounding surface at the image stress point is negative, which implies that if Eq. (6) is satisfied, the stress path reverses.

$$\frac{\partial F}{\partial \overline{s}_{ij}} ds_{ij} < 0 \tag{6}$$

The elastoplastic modulus gradually decreases to a certain value from the maximum value when the stress point moves from the initial loading point to the stress reversal point. Referring to the mapping rules (Dafalias and Herrmann 1986) related to the bounding surface theory, it is assumed that the initial loading point is the mapping centre on the loading path from the initial loading point to the stress reversal point. The elastoplastic modulus H of the current stress point is determined according to the elastoplastic modulus interpolation function represented as Eq. (7)

$$H = \left(\frac{\delta}{\delta_0} \right)^{\mu} H_{\max} \tag{7}$$

In Eq. (7), δ denotes the distance between the current stress point and the image stress point; δ_0 denotes the distance between the mapping centre and the image stress point; $H_{\max}$ represents the maximal elastoplastic modulus; the parameter μ reflects the accumulation rate and the level of shear strain.

The mapping rule of the first unloading is schematically shown in Fig. 1(b), where s'_R is the stress reversal point and starting point of the unloading path, $\overline{s}_k$ denotes the image stress point for unloading, and s_k denotes any point on the unloading stress path. The position of each point in the stress-strain curve is also shown in Fig. 1(c). We assume that the elastoplastic modulus at the beginning of the unloading is equal to the maximum $H_{\max}$ at the beginning of the initial loading. The stress reversal point is considered the mapping centre after stress reversing, and the elastoplastic modulus H of any stress point on the unloading path is determined according to Eq. (7).

Furthermore, for the reloading and subsequent re-unloading stress paths, the stress reversal points where the stress paths abruptly change direction are defined as the mapping centre. The elastoplastic modulus H of any stress point on the stress paths after reversing is determined according to Eq. (7).

Based on this description, the method to determine the hardening modulus for any stress point on cyclic loading paths is established, and the evolution rules of the hardening modulus field under cyclic loading are formed. When the elastoplastic modulus is determined using Eq. (7), the movement of the mapping centre creates a difference in elastoplastic modulus at the symmetrical position on the loading and unloading stress paths. Consequently, the cyclic hysteresis loop and strain accumulation of the soil element with initial static deviatoric stress is described.

2.3 Incremental elastoplastic relations

The strain increment includes two parts of the elastic and plastic strain increment. The elastic strain increment is obtained according to the generalised Hooke's law, and the plastic strain

increment is obtained according to the associative flow rule and bounding surface equation.

According to the radial mapping rules, the direction of plastic strain increment at the current stress points is assumed to be consistent with the normal direction of the bounding surface at the image stress points. Then, the plastic deviatoric strain increment is written as

$$\mathrm{d}e_{ij}^{\mathrm{p}} = \frac{1}{H'}\overline{n}_{ij}\overline{n}_{kl}\mathrm{d}s_{kl} \tag{8}$$

where $\mathrm{d}e_{ij}^{\mathrm{p}}$ is the plastic deviatoric strain increment; H' is the plastic shear modulus; $\overline{n}_{ij}$ and $\overline{n}_{kl}$ are the exterior normal unit vectors of the bounding surface at the image stress point; $\mathrm{d}s_{kl}$ is the deviatoric stress increment at the current stress point.

$$\overline{n}_{ij} = \frac{\partial F}{\partial \overline{s}_{ij}} \Bigg/ \sqrt{\frac{\partial F}{\partial \overline{s}_{kl}}\frac{\partial F}{\partial \overline{s}_{kl}}} = \sqrt{\frac{3}{2}}\frac{\overline{s}_{ij}}{A_0} \tag{9}$$

After substituting Eq. (9) into Eq. (8), we obtain Eq. (10)

$$\mathrm{d}e_{ij}^{\mathrm{p}} = \frac{3}{2H'}\frac{\overline{s}_{ij}}{A_0^{\,2}}\overline{s}_{kl}\mathrm{d}s_{kl} \tag{10}$$

According to the generalised Hooke's law, the elastic strain increment is obtained

$$\mathrm{d}e_{ij}^{\mathrm{e}} = \frac{\mathrm{d}s_{ij}}{2G} \tag{11}$$

where $\mathrm{d}e_{ij}^{\mathrm{e}}$ is the elastic deviatoric strain increment, and G is the elastic shear modulus.

The deviatoric strain increment is obtained from Eqs. (10) and (11)

$$\mathrm{d}e_{ij} = \frac{1}{2G}\mathrm{d}s_{ij} + \frac{3}{2H'}\frac{\overline{s}_{ij}}{A_0^{\,2}}\overline{s}_{kl}\mathrm{d}s_{kl} \tag{12}$$

where $\mathrm{d}e_{ij}$ is the deviatoric strain increment.

For the torsional shear stress state without axial deviatoric stress (refer to Fig. 8), the circumferential shear strain and axial strain increments are obtained as follows by simplifying Eq. (12)

$$d\gamma_{z\theta} = (\frac{1}{G} + \frac{2}{H'})d\tau_{z\theta} = \frac{2}{H}d\tau_{z\theta} \tag{13}$$

$$d\varepsilon_z = 0 \tag{14}$$

where $d\varepsilon_z$ is the axial strain increment, and $d\gamma_{z\theta}$ is the circumferential shear strain increment.

For the undrained triaxial stress state, the axial strain increment is obtained as Eq. (15) by simplifying Eq. (12)

$$\mathrm{d}\varepsilon_z = \frac{2}{3}\left(\frac{1}{2G} + \frac{1}{H'}\right)\mathrm{d}\sigma_R = \frac{2}{3H}\mathrm{d}\sigma_R \tag{15}$$

where H is the elastoplastic modulus and obeys the following relation

$$\frac{1}{H}=\frac{1}{2G}+\frac{1}{H'} \tag{16}$$

At the beginning of initial loading, we believe that only the elastic strain is produced, whereas the plastic modulus is infinite, so the maximum of elastoplastic modulus is

$$H_{\max}=2G \tag{17}$$

3. Model parameters

The developed model requires three undetermined parameters: radius of the bounding surfaceA_0, elastic shear modulus G and parameter μ, which reflects the accumulation rate and the level of shear strain.

All model parameters are determined using undrained cyclic triaxial compression tests. Because parameter μ is associated with the static and cyclic stress levels of soil elements, and the stress level of soil elements in the general stress states can be represented using the octahedral shear stress τ_8, parameter μ is expressed as the function of the octahedral static shear stress ratio $\tau_{8,a}/\tau_{8,f}$ and cyclic shear stress ratio $\tau_{8,cy}/\tau_{8,f}$. Here, the octahedral static shear stress $\tau_{8,a}$ is defined as the octahedral shear stress of the soil element under static loading. The octahedral cyclic shear stress $\tau_{8,cy}$ is defined as one half of the octahedral shear stress variation amount of the soil element under static and cyclic loading. In addition, the octahedral peak shear stress $\tau_{8,f}$ is defined as the octahedral shear stress when the sample reaches the deformation failure criteria. If the soil elements are in the triaxial stress states, the octahedral shear stress and strain are represented by Eqs. (18) and (19), respectively.

$$\tau_8=\sqrt{2}\left(\sigma_z-\sigma_\theta\right)/3 \tag{18}$$

$$\gamma_8=\sqrt{2}\varepsilon_z \tag{19}$$

where σ_z, σ_θ and ε_z denote the axial stress, circumferential stress and axial strain.

3.1 Triaxial compression tests

Reconstituted soft clay was used in the experiment. The basic physical index of the soil samples are shown in Table 1.

The initial size of the samples is 8.0 cm in height and 3.91 cm in diameter. The HX-100 Electric Servo Control Triaxial Apparatus was used in these experiments. Then, unconsolidated undrained static and cyclic triaxial compression tests were performed under the stress-

Table 1 Basic physical indexes of the soil samples

Unit weight (kN/m^3)	Water content (%)	Plastic limit	Liquid limit	Plastic index
16.2	31.0	21	45	24

Table 2 Static and cyclic stress ratios for the cyclic triaxial compression tests

$\tau_{8,a}/\tau_{8,f}$	$\tau_{8,cy}/\tau_{8,f}$	$\tau_{8,a}/\tau_{8,f}$	$\tau_{8,cy}/\tau_{8,f}$	$\tau_{8,a}/\tau_{8,f}$	$\tau_{8,cy}/\tau_{8,f}$
0.3	1.577	0.5	1.087	0.7	1.022
0.3	0.412	0.5	0.494	0.7	0.280
0.3	0.323	0.5	0.423	0.7	0.215
0.3	0.263	0.5	0.358	0.7	0.183
0.3	0.227	0.5	0.310	0.7	0.165
0.3	0.152	0.5	0.181	0.7	0.120

controlled condition. The confining pressure that was applied to the sample is 100 kPa during the experiment.

The following tests were performed:

Unconsolidated undrained static triaxial compression tests. The static compression strength σ_f was determined according to these tests. σ_f is the axial deviatoric stress when the axial strain of sample reaches 10%. The obtained results are: σ_f is 25 kPa, and the corresponding $\tau_{8,f}$ is 11.79 kPa.

Unconsolidated undrained cyclic triaxial compression tests under the joint actions of different static and cyclic stress. By performing these tests, the radius of the bounding surface A_0, shear modulus G and parameter μ were determined.

The octahedral static shear stress ratio and cyclic shear stress ratio were defined as $\tau_{8,a}/\tau_{8,f}$ and $\tau_{8,cy}/\tau_{8,f}$, respectively, to represent the static deviatoric stress level and cyclic stress level that were applied to the sample during the experiment. For each $\tau_{8,a}/\tau_{8,f}$, different $\tau_{8,cy}/\tau_{8,f}$ values were selected to do the tests, as shown in Table 2.

The main experimental steps are as follows:

(1) 100 kPa confining pressure was applied to the sample after setting it in the triaxial cell.
(2) Axial static deviatoric stress was applied to the sample under unconsolidated undrained condition.
(3) A 0.1 Hz sinusoidal constant-amplitude cyclic deviatoric stress was not exerted until there was a relatively stable axial deformation.

The static and cyclic stress ratios that corresponded to the cyclic triaxial compression tests under high cyclic stress level are shown in the second line of Table 2. These tests were used to determine the radius of bounding surface A_0 and shear modulus G. For the effect of the loading rate, the compression strength and shear modulus of the soil element under cyclic loading are different from those under static loading when they reach the identical deformation failure criteria. To consider the loading rate effect, the cyclic triaxial compression tests under high cyclic stress level with different initial static stress level were performed. In these tests, $\tau_{8,a}/\tau_{8,f}$ are set as 0.3, 0.5 and 0.7. A larger cyclic stress amplitude (the axial deformation is beyond 10% after loading for a quarter cycle) was selected for each $\tau_{8,a}/\tau_{8,f}$. The tests were finished after loading for a cycle.

Cyclic triaxial compression tests that corresponded to other static and cyclic stress ratios in Table 2 were used to determine the parameter μ. The tests were finished if the sum of octahedral static shear strain and octahedral cyclic accumulative shear strain was over 14.1% after applying the cyclic stress to the sample. Fig. 2 shows the typical stress-strain curves obtained from the test results; $\gamma_{8,a}$ is the octahedral static shear strain caused by the octahedral static shear stress $\tau_{8,a}$; $\gamma_{8,p}$ is the octahedral cyclic accumulative shear strain caused by octahedral cyclic stress $\tau_{8,cy}$; $\Delta\gamma_{8,p}$ is the octahedral cyclic accumulative shear strain increment after each loading cycle.

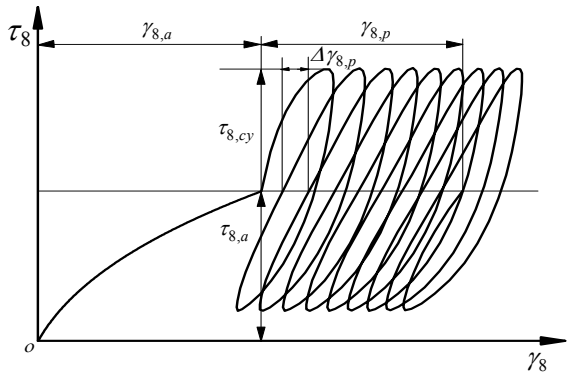

Fig. 2 Typical stress-strain curve for cyclic triaxial compression tests with the initial axial deviatoric stress

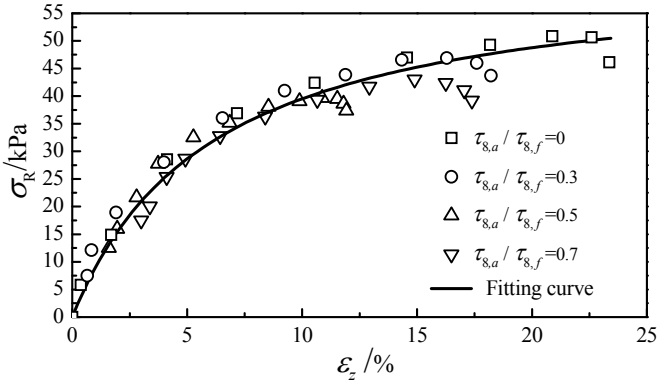

Fig. 3 Initial stress-strain response curves with different static stress ratios

3.2 Parameters A_0 and G

Fig. 3 shows the initial loading curve that was obtained from the cyclic triaxial tests under high cyclic stress level with different static stress ratios. These results indicate that their initial stress-strain responses follow the same initial loading curve, although the octahedral static shear stress ratios are different. According to bounding surface Eq. (5) in the triaxial stress states, the axial deviatoric stress $\overline{\sigma}_R$ when the soil sample is damaged is the radius of bounding surface A_0, which was determined using the failure criteria of reaching 10% axial strain, and the result is A_0 = 39.5 kPa. Obviously, for the effect of the loading rate, the compression strength of the soil element under cyclic loading (for a quarter cycle) is bigger than that under static loading when they reach the identical deformation failure criteria.

Furthermore, to determine the tangential modulus E of the initial loading, the stress-strain curves were fitted using Eq. (20). Its value is 1/a. The shear modulus G was determined using Eq. (21), and the obtained value is 347 kPa.

$$\sigma_R = \varepsilon_z / \left(a + b\varepsilon_z\right) \tag{20}$$

where a and b are undetermined coefficients; the values obtained from the fitting results are a = 0.00096 and b = 0.0157

$$G = E/2(1+\nu) \tag{21}$$

where v denotes the Poisson's ratio, and its value is 0.5 under undrained condition.

3.3 Parameter μ

To reflect the effects of the stress history on the accumulative strain, parameter μ is shown in Eq. (22)

$$\mu = \mu_0 d\gamma_{8,p} \tag{22}$$

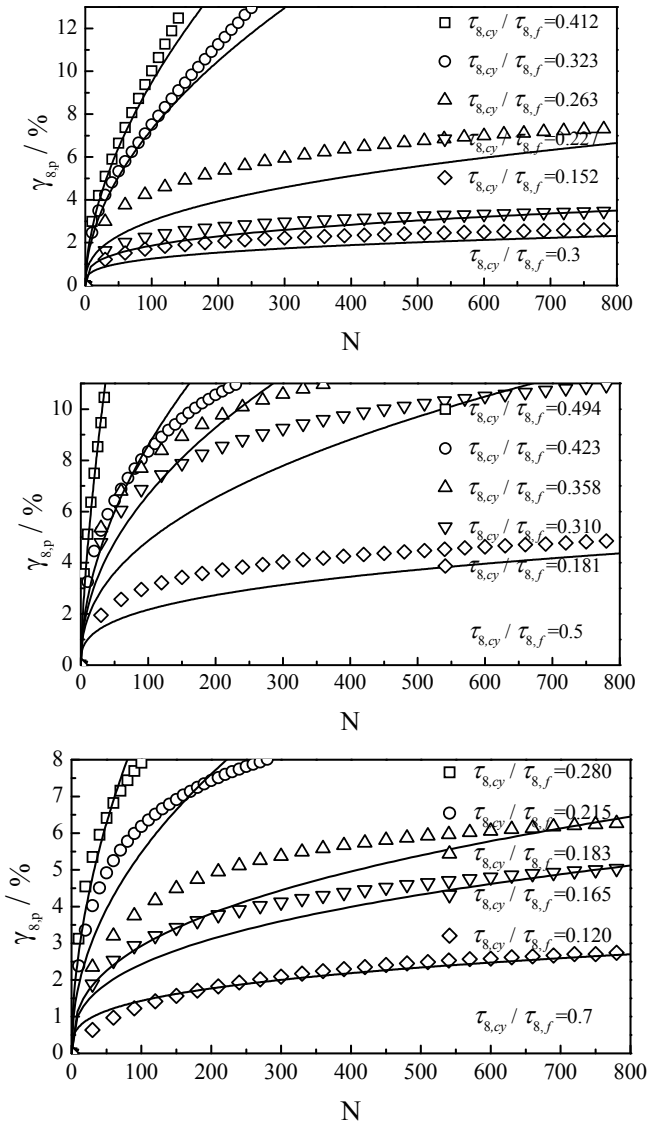

Fig. 4 Octahedral cyclic accumulative shear strain versus the number of stress cycles in triaxial compression tests

where $d\gamma_{8,p}$ denotes the octahedral accumulative shear strain increment after every stress cycles, which depends on the stress history and current cyclic stress level, and controls the trends of the accumulative shear strain versus the number of stress cycles; the coefficient μ_0 controls the level of the accumulative shear strain after a certain number of stress cycles.

Fig. 4 shows the octahedral cyclic accumulative shear strain versus the number of stress cycles using discrete symbols, which were obtained using undrained cyclic triaxial compression tests with three groups of octahedral static shear stress ratios and cyclic shear stress ratios. Experimental data were fitted using Eq. (23), and the fitting results are presented with solid lines in Fig. 4. The octahedral cyclic accumulative shear strain increment is shown in Eq. (24), which was obtained using Eq. (23).

$$\gamma_{8,p} = cN^d \tag{23}$$

where c and d are coefficients of the fitting function, and their values are listed in Table 3, N is the number of stress cycles.

$$d\gamma_{8,p} = cdN^{d-1} \tag{24}$$

The c and d values versus $\tau_{8,cy}/\tau_{8,f}$ for given $\tau_{8,a}/\tau_{8,f}$ were fitted using Eqs. (25) and (26) separately, as shown in Fig. 5. The coefficients k_1 and k_2 were fitted using Eqs. (27) and (28) separately, as shown in Fig. 6. The c and d values for any given $\tau_{8,a}/\tau_{8,f}$ and $\tau_{8,cy}/\tau_{8,f}$ can be determined by the Eqs. (25)-(28).

$$c = k_1 \tau_{8cy}/\tau_{8f} \tag{25}$$

$$d = k_2 \tau_{8cy}/\tau_{8f} \tag{26}$$

$$k_1 = 1.804 + 1.139\tau_{8a}/\tau_{8f} - 5.559\left(\tau_{8a}/\tau_{8f}\right)^2 + 8.621\left(\tau_{8a}/\tau_{8f}\right)^3 \tag{27}$$

$$k_2 = 1.202 + 1.071\tau_{8a}/\tau_{8f} - 4.618\left(\tau_{8a}/\tau_{8f}\right)^2 + 6.947\left(\tau_{8a}/\tau_{8f}\right)^3 \tag{28}$$

μ_0 can be determined using the following trial calculation method after obtaining $d\gamma_{8,p}$:

For a given incremental deviatoric stress, first, by assuming that a μ_0, μ can be determined

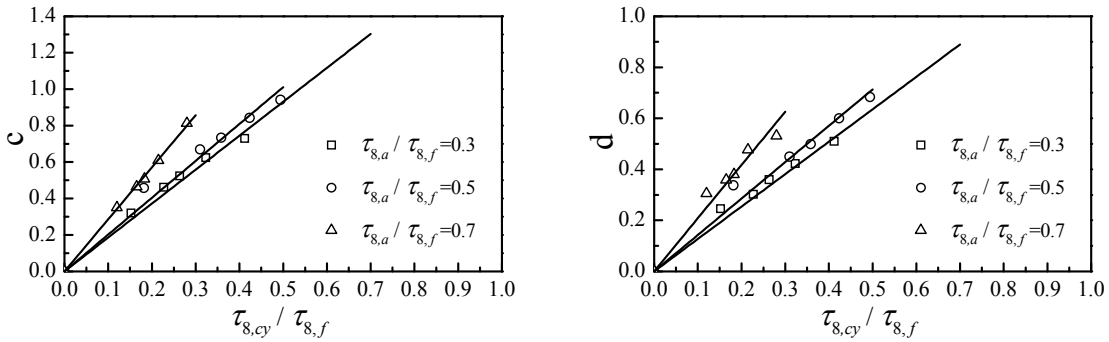

Fig. 5 c and d values versus $\tau_{8,cy}/\tau_{8,f}$ for given $\tau_{8,a}/\tau_{8,f}$

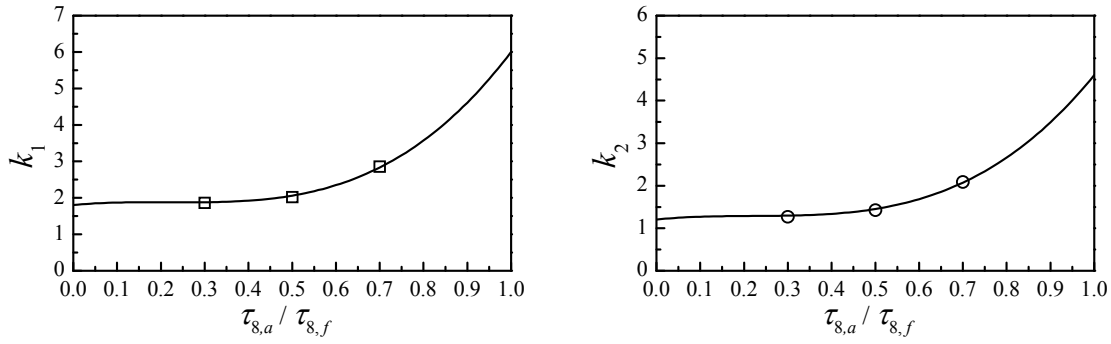

Fig. 6 k_1 and k_2 values versus $\tau_{8,a} / \tau_{8,f}$

according to Eq. (22), the elastoplastic modulus of the current stress points is determined using Eq. (7). Second, the incremental strain that corresponds to the incremental stress can be calculated using Eq. (15). As a result, the axial cyclic deviatoric stress-strain curve of the triaxial sample can be obtained. For cyclic failure tests, it is necessary to determine the number of stress cycles (the number of cyclic failure) according to the calculation results when the sum of octahedral static shear strain and octahedral cyclic accumulative shear strain reach 14.1%. If the determined number of stress cycles is inconsistent with the triaxial test results, μ_0 must be adjusted to repeat the above process until the calculation results are consistent with the experimental results. For the tests where the total strain does not satisfy the failure criterion, it is necessary to determine the accumulative strain that corresponds to the maximum number of stress cycles according to the calculation results of stress-strain curve, then the calculation and test results of accumulative strain are compared. If they are inconsistent, μ_0 must be adjusted to repeat the above process until the

Table 3 Parameters c, d and μ_0 with different static and cyclic stress ratios

$\tau_{8,a} / \tau_{8,f}$	$\tau_{8,cy} / \tau_{8,f}$	c	d	μ_0
0.3	0.412	0.7295	0.5099	3.65
0.3	0.323	0.6250	0.4233	6.45
0.3	0.263	0.5252	0.3599	9.05
0.3	0.227	0.4625	0.3027	13.35
0.3	0.152	0.3205	0.2460	25.05
0.5	0.494	0.9416	0.6836	1.82
0.5	0.423	0.8423	0.6001	1.95
0.5	0.358	0.7343	0.4987	2.6
0.5	0.310	0.6699	0.4500	3.75
0.5	0.181	0.4580	0.3373	10.5
0.7	0.280	0.8135	0.5319	1.5
0.7	0.215	0.6085	0.4769	4.2
0.7	0.183	0.5083	0.3801	6.3
0.7	0.165	0.4655	0.3586	7.7
0.7	0.120	0.3510	0.3053	14.2

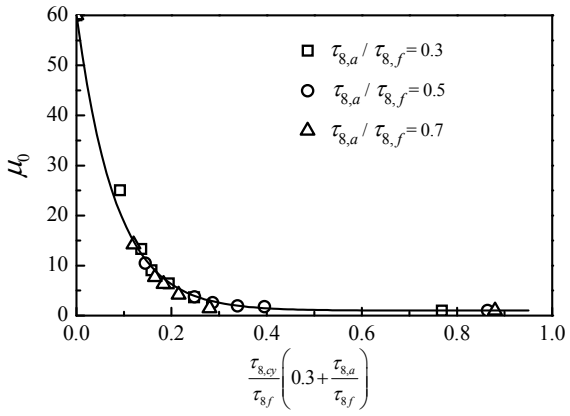

Fig. 7 Parameter μ_0 with different static and cyclic stress ratios

results are consistent. The μ_0 values that are determined in this manner are shown in Table 3.

$$\mu_0 = 1 + 59.24 \times (5.625\mathrm{E}-6)^{\frac{\tau_{8,cy}}{\tau_{8,f}}\left(0.3+\frac{\tau_{8,a}}{\tau_{8,f}}\right)} \tag{29}$$

The triaxial compression strength of the soil element under cyclic loading (for a quarter cycle) is 1.58 times bigger than that under static loading (the former is 39.5kPa and the latter is 25 kPa). Therefore, for these tests in this article, the maximum value of the sum of the octahedral static shear stress ratio and cyclic shear stress ratio is 1.58. It is observed that μ_0 decreases monotonically with the increase of the octahedral cyclic shear stress ratio when the octahedral static shear stress ratio remains constant in Fig. 7. μ_0 approaches a certain value (It is 60 for these tests) when the cyclic shear stress ratio approaches zero, whereas the cyclic accumulative strain of soil element approaches zero. μ_0 approaches 1 when the sum of the octahedral static shear stress ratio and cyclic shear stress ratio approaches the maximum value (It is 1.58 for these tests), which implies that a larger cyclic accumulative strain is produced with fewer stress cycles. μ_0 for any static stress ratio and cyclic stress ratio can be obtained by the Eq. (29).

4. Verification of the model performance

To verify the prediction capability of the proposed model, triaxial extension and torsional shear tests that were subjected to the different combinations of initial and cyclic stresses were performed for the clays. Then, the test results were predicted using the proposed model. First, the cyclic triaxial extension and torsional shear tests were introduced; then, the predicted results and test results were compared.

4.1 Laboratory experiments

Two groups of tests were performed and numbered as S1, S2: cyclic triaxial extension tests and cyclic torsional shear tests respectively. The initial octahedral static shear stress ratio and octahedral cyclic shear stress ratio that were applied to the sample are shown in Table 4. The soft

clay in the following tests is identical to that in the aforementioned triaxial compression tests.

(1) Cyclic triaxial extension tests (S1). The tests remain stress-controlled, the initial size of sample and test procedures are basically identical to the aforementioned triaxial compression tests. The difference is: the initial static deviatoric stress was applied to the soil sample in the direction of extension, and a 0.1 Hz sinusoidal constant-amplitude cyclic deviatoric stress was not exerted until there was a relative stable axial deformation. Finally, the test was finished if the sum of octahedral static shear strain and octahedral cyclic accumulative shear strain was over 14.1%.

(2) Cyclic torsional shear tests (S2). The tests were performed using a Vertical-Torsional Coupling Shear Apparatus. The hollow cylinder samples were used in the tests with the following initial size: inner diameter 3 cm, external diameter 7 cm, and height 10 cm. The unconsolidated undrained torsional shear tests were conducted under stress-controlled condition after applying an isotropic confining pressure to the sample.

The main experimental procedures are as follows:

(1) The prepared hollow cylinder sample was placed in the pressure chamber, and 100 kPa confining pressure was subsequently applied to that after connecting the sealed rubber membrane in the inner and outer walls of the pressure chamber.

Table 4 Static and cyclic stress ratio of tests with different stress states

Test number	Tests with different stress states	$\tau_{8,a}/\tau_{8,f}$	$\tau_{8,cy}/\tau_{8,f}$
S1	Triaxial extension tests	0.5	0.495
		0.5	0.451
		0.5	0.250
		0.5	0.205
S2	Torsional shear tests	0.3	0.248
		0.3	0.270
		0.3	0.301
		0.3	0.504

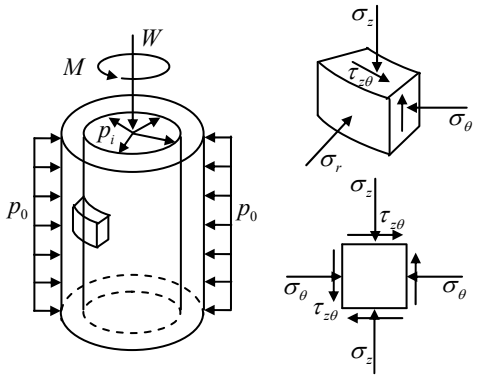

Fig. 8 Stress state of the sample in the torsional shear tests

(2) An initial circumferential static torque was applied to the sample; The initial static stress level was represented with the octahedral static shear stress ratio $\tau_{8,a}/\tau_{8,f}$, whose values are shown in Table 4.
(3) A 0.1 Hz sinusoidal constant-amplitude circumferential cyclic torque was applied to the soil sample after reaching a relative stable circumferential deformation. The cyclic stress level was represented with the octahedral cyclic shear stress ratio $\tau_{8,cy}/\tau_{8,f}$. The tests were performed by choosing different $\tau_{8,cy}/\tau_{8,f}$ for each $\tau_{8,a}/\tau_{8,f}$. The tests were finished when the sum of octahedral static shear strain and cyclic accumulative shear strain was over 14.1%.

The stress state of the soil samples is illustrated in Fig. 8. M denotes the cyclic torque that was applied to the end of the sample, W denotes the axial load, p_i denotes the inner pressure, p_0 denotes the outer pressure, σ_z denotes the axial stress, σ_θ denotes the circumferential stress, σ_r denotes the radial stress, and $\tau_{z\theta}$ denotes the circumferential shear stress.

For S2, the axial stress that was applied to the sample is equal to the confining pressure, i.e., without axial deviatoric stress. When a static torque and a cyclic torque are applied to the end of the sample, $\sigma_z = \sigma_r = \sigma_\theta$, $\tau_{rz} = \tau_{r\theta} = 0$, for this stress state, the corresponding bounding surface equation is Eq. (3), the circumferential shear strain increment and axial strain increment can be obtained using Eqs. (13) and (14), respectively. The stress paths of the soil element with two different stress states S1, S2 can be seen from Fig. 1. For S1, the stress point always make a reciprocating movement along the σ_R-axis. For S2, the stress point always make a reciprocating movement along the τ_{xy}-axis.

4.2 Prediction for the triaxial extension tests results

Fig. 9 shows the experimental results and model predictions of the axial cyclic accumulative strain $\varepsilon_{z,p}$ versus the number of stress cycles N in the S1 tests with discrete symbols and continuous lines, respectively. The consistency among the data is relatively satisfactory. Therefore, based on the model parameters determined by the cyclic triaxial compression tests, using the proposed model, the variation tendency of $\varepsilon_{z,p}$ versus N in the triaxial extension tests can be predicted for the tested clays.

Furthermore, the axial stress-strain curves of the soil sample in the S1 tests were simulated. The test results and predicted results are shown in Fig. 10, which shows that the model can describe the cyclic hysteresis loop and axial strain accumulation of stress-strain curves. However, the predicted hysteresis hoop is relatively smaller than that of the actual tests.

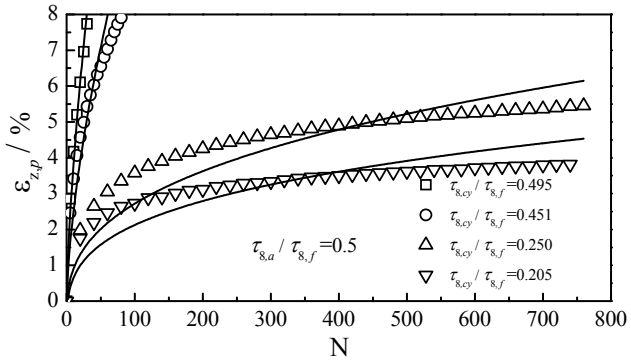

Fig. 9 Axial cyclic accumulative strain versus the number of stress cycles in the triaxial extension tests

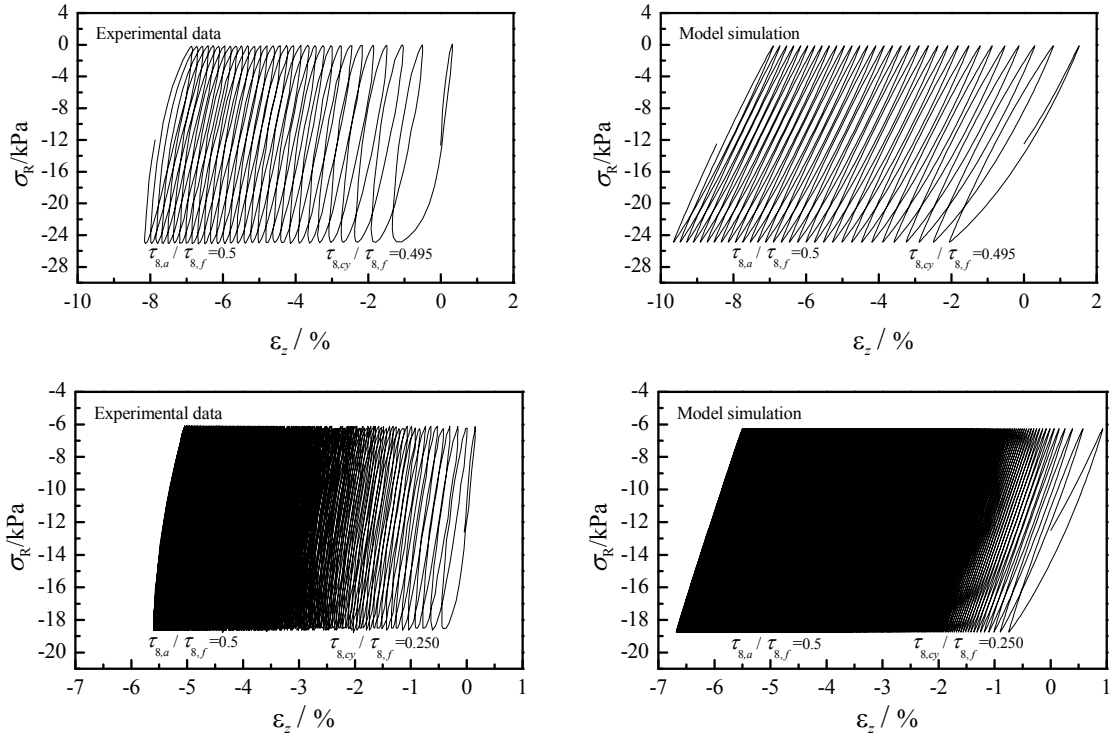

Fig. 10 Comparison of axial stress-strain curves between the test and forecast results in the triaxial extension tests

4.3 Prediction for the torsional shear test results

The experimental results show that when there is an initial torque, the circumferential cyclic torque only causes the accumulation of circumferential shear strain instead of axial strain. Fig. 11 shows the experimental results and model predictions of the circumferential cyclic accumulative shear strain $\gamma_{z\theta,p}$ versus the number of stress cycles N using discrete symbols and continuous lines, respectively. It is observed that $\gamma_{z\theta,p}$ increases with the increase of cyclic stress level under the same initial static stress level. The result is similar to the triaxial extension tests, the soil element exhibits cyclic shakedown or cyclic failure states with different cyclic stress levels. The comparative results indicate that the model can basically predict the trend of $\gamma_{z\theta,p}$ versus N.

Fig. 12 shows the experimental results and model predictions of the circumferential stress - strain hysteresis curve. It is observed that the model can describe the cyclic hysteresis loop and circumferential strain accumulation of soil elements under different cyclic stress levels for the tested clays. However, the predictive hysteresis loop is relatively smaller than that of the real tests, which is similar to the prediction results of triaxial extension tests. Furthermore, according to Eq. (14), the axial strain is always zero under circumferential cyclic torque without axial deviatoric stress, which is consistent with the test results. In fact, for S1 and S2, the stress point moves along the σ_R-axis and $\tau_{x,y}$-axis, respectively(see Fig. 1). The change rule of stress paths and hardening modulus are similar. Thus, the stress-strain responses of the soil elements with two different stress states are similar.

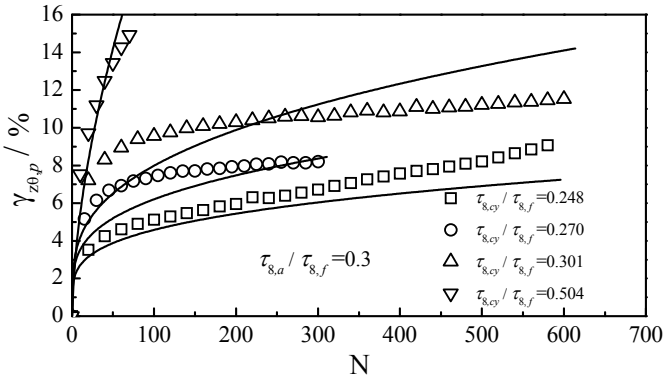

Fig. 11 Circumferential cyclic accumulative shear strain versus the number of stress cycles

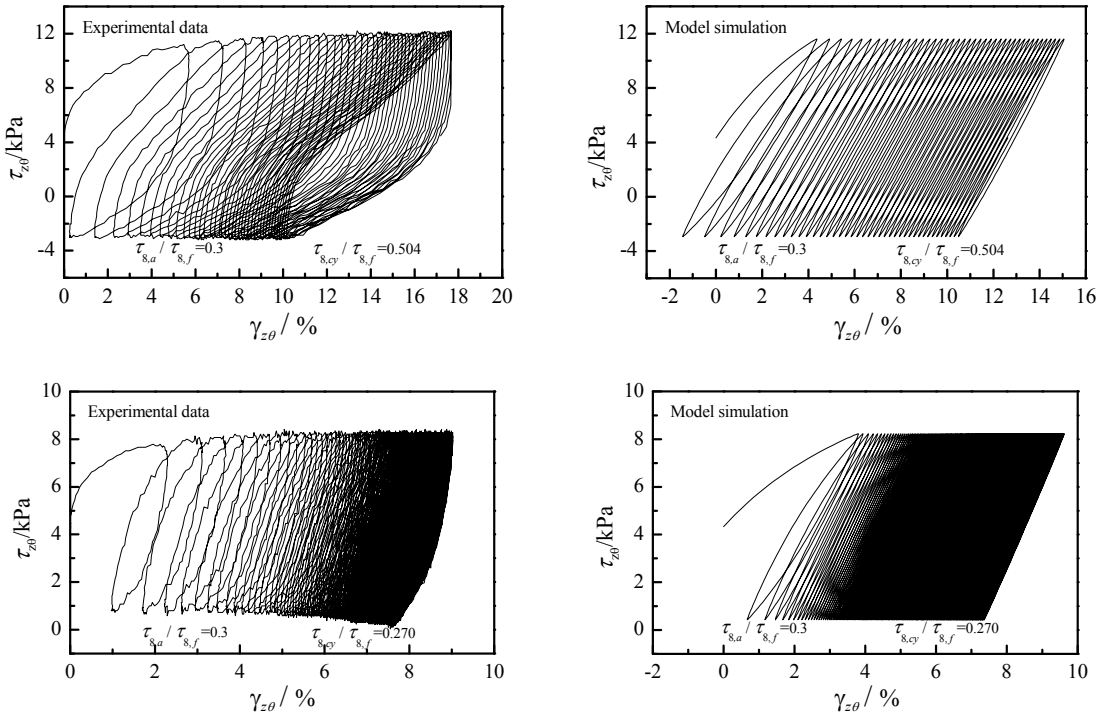

Fig. 12 Comparison of circumferential stress-strain curves between the test and the forecast results

5. Conclusions

A total stress-based elastoplastic constitutive model has been developed to predict the behaviour of saturated soft clays under cyclic loads. Furthermore, the model parameters were determined according to cyclic triaxial compression tests. Then, the applicability of the proposed model was verified by comparing its predictions with the cyclic triaxial extension and torsional shear test results. The key conclusions can be summarized as follows:

(1) A new hardening rule is developed based on a new interpolation function of the hardening modulus that has simple mathematic expression and fewer model parameters. Cyclic stress-strain hysteresis curve can be described based on the new hardening rule. In addition, because a model parameter that reflects the accumulation rate and level of shear strain is introduced to the interpolation function, the proposed model can capture the cyclic shakedown and failure behaviour of soil elements with different initial and cyclic stress levels.
(2) The model parameters can be determined according to the cyclic triaxial compression tests. To apply the model to the numerical analysis of boundary value problems, the octahedral shear stress can be used to represent the stress level of soil elements in general stress states. Besides, because some model parameters are associated with stress level of soil elements, they can be expressed as the function of the octahedral static shear stress ratio and cyclic shear stress ratio.
(3) The model predictions are in relatively good agreement with the cyclic triaxial tensile and torsional shear test results, despite some deviations, which indicate that the model has good applicability for elements of the tested clays with different stress states.
(4) Although the phenomena such as pore-pressure buildup and dissipation cannot be captured, it is believed that the new model provides the simplicity that is very much needed for practical implementation into 3D nonlinear finite-element analysis codes. Further work along this direction with numerical implementation is in progress.

Acknowledgments

Financial support from the National Natural Science Foundation of China (Grant No. 51179120) and the Special Research Fund for the Doctoral Program of Higher Education (Grant No. 20130032110045) is gratefully acknowledged.

References

Anastasopoulos, I., Gelagoti, F., Kourkoulis, R. and Gazetas, G. (2011), "Simplified constitutive model for simulation of cyclic response of shallow foundations: Validation against laboratory tests", *J. Geotech. Geoenviron. Eng., ASCE*, **137**(12), 1154-1168.

Anderson, K.H. (2009), "Bearing capacity under cyclic loading-offshore, along the coast, and on land", *Can. Geotech. J.*, **46**(5), 513-535.

API RP2A-WSD (2002), Recommended practice for planning, designing, and constructing fixed offshore platforms-working stress design; American Petroleum Institute, Houston, TX, USA.

Borja, R.I. and Amies, A.P. (1994), "Multiaxial cyclic plasticity model for clays", *J. Geotech. Eng.*, **120**(6), 1051-1070.

Chen, W. and Randolph, M.F. (2007), "Uplift capacity of suction caissons under sustained and cyclic loading in soft clay", *J. Geotech. Geoenviron. Eng.*, **133**(11), 1352-1363.

Crouch, R.S. and Wolf, J.P. (1994), "Unified 3D critical state bounding-surface plasticity model for soils incorporating continuous plastic loading under cyclic paths", *Int. J. Numer. Anal. Method. Geomech.*, **18**(11), 735-784.

Dafalias, Y.F. and Herrmann, L.R. (1982), "A generalized bounding sufrace constitutive model for clays", *Application of Plasticity and Generalized Stress-Strain in Geotechnical Engineering*, *Proceedings of the Symposium on Limit Equilibrium*, *Plasticity*, *and Generalized Stress Strain Applications in Geotechnical*

Engineering, *ASCE*, Hollywood, FL, USA, October, pp. 78-95.
Dafalias, Y.F. and Herrmann, L.R. (1986), "Bounding surface plasticity. Part II: Application to isotropic cohesive soils", *J. Eng. Mech.*, **112**(12), 1263-1291.
Hong, P.Y., Pereira, J.M., Cui, Y.J., Tang, A.M., Collin, F. and Li, X.L. (2014), "An elastoplastic model with combined isotropic-kinematic hardening to predict the cyclic behavior of stiff clays", *Comput. Geotech.*, **62**, 193-202.
Hu, C., Liu, H.X. and Huang, W. (2012), "Anisotropic bounding-surface plasticity model for the cyclic shakedown and degradation of saturated clay", *Comput. Geotech.*, **44**, 34-47.
Huang, M.S. and Liu, Y. (2014), "Numerical analysis of axial cyclic degradation of a single pile in saturated soft soil based on nonlinear kinematic hardening constitutive model", *Chinese J. Geotech. Eng.*, **36**(12), 2170-2178.
Huang, M.S., Liu, M and Liu, Y.H. (2009), "Anisotropic bounding surface model for saturated soft clay under cyclic loading", *J. Hydraul. Eng.*, **40**(2), 188-193.
Huang, M.S., Liu, Y.H. and Sheng, D.C. (2011), "Simulation of yielding and stress-strain behavior of shanghai soft clay", *Comput. Geotech.*, **38**(3), 341-353.
Kimoto, S., Shahbodagh Khan, B., Mirjalili, M. and Oka, F. (2013), "Cyclic elastoviscoplastic constitutive model for clay considering nonlinear kinematic hardening rules and structural degradation", *Int. J. Geomech., ASCE*, **15**(5), A4014005.
Li, G.X. (2004), *Advanced Soil Mechanics*, Tsing Hua University Publishing House, Beijing, China.
Li, T. and Meissner, H. (2002), "Two-surface plasticity model for cyclic undrained behavior of clays", *J. Geotech. Geoenviron. Eng., ASCE*, **128**(7), 613-626.
Liang, R.Y. and Ma, F.G. (1992), "Anisotropic plasticity model for undrained cyclic behavior of clays", *J. Geotech. Eng., ASCE*, **118**(2), 229-265.
Mroz, Z., Norris, V.A. and Zienkiewicz, O.C. (1981), "An anisotropic, critical state model for soils subject to cyclic loading", *Geotechnique*, **31**(4), 451-469.
Ni, J., Indraratna, B., Geng, X.Y., Carter, J.P. and Chen, Y.L. (2015), "Model of soft soils under cyclic loading", *Int. J. Geomech.*, **15**(4), 04014067
Pande, G.N. and Pietruszczak, S. (1982), "Reflecting surface model for soils", *Proceedings of International Symposium on Numerical Models in Geomechanics*, Zurich, Switzerland.
Prevost, J.H. (1977), "Mathematical modelling of monotonic and cyclic undrained clay behaviour", *Int. J. Numer. Anal. Method. Geomech.*, **1**(2), 195-216.
Seidalinov, G. and Taiebat, M. (2014), "Bounding surface SANICLAY plasticity model for cyclic clay behaviour", *Int. J. Numer. Anal. Method. Geomech.*, **38**(7), 702-724.
Tabbaa, A.Al. and Wood, D.M. (1989), "An experimentally based "bubble" model for clay", *Proceedings of the 3rd International Symposium on Numerical Models in Geomechanics*, Niagara Falls, Canada, May.
Wang, J.H. and Qu, Y.D. (2011), "Unconsolidated and undrained strength and failure criterion of soft clay under cyclic stresses", *J. Hydraul. Eng.*, **42**(6), 672-677.
Wang, J.H. and Yao, M.l. (1996), "Elastoplastic simulation of the cyclic undrained behaviour of soft clays", *Chinese J. Geotech. Eng.*, **18**(3), 11-18.
Xiong, Y.C. and Chen, J.Z. (2008), "Cyclic elasto-plastic constitutive model considering anisotropic effect", *Chinese J. Geotech. Eng.*, **30**(8), 1165-1170.
Yin, Z.Y., Xu, Q. and Hicher, P.Y. (2013), "A simple critical-state-based double-yield-surface model for clay behavior under complex loading", *Acta Geotechnica*, **8**(5), 509-523.
Yu, H.S., Khong, C. and Wang, J. (2007), "A unified plasticity model for cyclic behaviour of clay and sand", *Mech. Res. Commun.*, **34**(2), 97-114.

CC